

# Evolution, Collapse, and Recovery of Electronically Conductive Networks in Sulfide-Based All-Solid-State Batteries Using Passivation-Coated NMC and C65

Nikolaos Papadopoulos, Elias Reisacher,\* Tim Schubert, Simon Hein, Timo Danner, Arnulf Latz, Pinar Kaya,\* and Volker Knoblauch\*

All-solid-state batteries offer enhanced safety and energy density compared to conventional systems, but their performance critically depends on the microstructure of the composite cathode. Sulfide-based solid electrolytes (SEs) are promising Li-ion conductors, yet they degrade upon contact with cathode active materials, necessitating passivating coatings that impair electronic conductivity. Herein, an electron-conducting matrix of SE and 4 wt% conductive additive (C65) at the percolation threshold is introduced to minimize side reactions. The effect of coated active material fraction on ionic and electronic conductivities is investigated using electrochemical impedance spectroscopy, rate tests, 2D/3D imaging,

and numerical simulations. The results highlight the critical role of the electronically conductive network, which percolates at low CAM loadings, collapses at 50 wt% as C65 adheres to coated CAM surfaces—depleting the bulk network—and recovers at higher loadings via percolation of C65-coated particles, demonstrating the essential function of C65. At 70 wt%, a robust network yields 99.8 mAh g<sup>-1</sup> at C/10 and 84% retention at C/5; at 80 wt%, ionic conductivity diminishes despite improved electronic transport, reducing rate performance. These findings underscore the need to balance ionic and electronic pathways and provide new insights into the role of additives in composite cathodes.

## 1. Introduction

Battery systems are a crucial enabling technology for the transition from fossil fuels to sustainable energy. All-solid-state batteries (ASSBs) have emerged as a promising alternative to conventional liquid electrolyte-based batteries due to their potential for enhanced safety and higher energy density through the use of lithium metal anodes.<sup>[1–4]</sup> These potentials stimulated intense research efforts in recent years, with the aim of

overcoming the remaining technical challenges and moving solid-state technology toward practical applications.<sup>[5]</sup>

Composite cathodes (CCs) exhibit a complex microstructure and are critical to overall electrochemical performance. They typically consist of a solid electrolyte (SE) and a cathode active material.<sup>[6,7]</sup> Generally, in such two-phase cathode microstructures, the SE provides the ionic charge transport, whereby the active material and conductive additive (CA) are responsible for the electronic charge transport.<sup>[7]</sup> The two phases are usually inversely isolating for the complementary charge species in the CC.<sup>[5,7,8]</sup> Among lithium-ion conductors, sulfide SEs have the highest conductivities at room temperature, outperforming polymers or oxide electrolytes.<sup>[9]</sup> In particular, these types of SEs combine the advantages of relatively simple synthesis with high ionic conductivity.<sup>[10,11]</sup> Among them, the chlorine-doped argyrodite Li<sub>6</sub>PS<sub>5</sub>Cl (LPSCl) is a highly promising representative with high ionic conductivity utilizing relatively cheap raw materials.<sup>[10,12]</sup> However, sulfide SEs tend to decompose when in contact with the active materials on both the positive and negative electrodes.<sup>[13–16]</sup>

Thus, to utilize thiophosphates and prevent degradation at the SE-NMC interface, it is necessary to apply thin oxide coatings such as Li<sub>4</sub>TiO<sub>3</sub>, ZrO<sub>2</sub>, and LiNbO<sub>3</sub> on the NMC particles.<sup>[14,16]</sup> However, while being permeable for the lithium ions, these coatings impair the electronic conductivity since they are poor electronic conductors.<sup>[13]</sup> One approach to overcome the poor electronic conductivity of coated active material is to add CAs to the CC.<sup>[17]</sup> However, it is known that the addition of these additives can lead to accelerated degradation at the CA-SE interface and deteriorate the cycle life.<sup>[18,19]</sup>

In their investigation of two-phase mixtures in blocking configurations, Minnmann et al. employed NMC622 (intrinsic

N. Papadopoulos, E. Reisacher, T. Schubert, P. Kaya, V. Knoblauch  
Materials Research Institute (IMFAA)  
Aalen University of Applied Sciences  
Beethovenstraße 1, 73430 Aalen, Germany  
E-mail: elias.reisacher@hs-aalen.de  
pinar.kaya@hs-aalen.de  
volker.knoblauch@hs-aalen.de

S. Hein, T. Danner, A. Latz  
Institute of Engineering Thermodynamics  
German Aerospace Center (DLR)  
Pfaffenwaldring 38-40, 70569 Stuttgart, Germany

S. Hein, T. Danner, A. Latz  
Helmholtz Institute Ulm for Electrochemical Energy Storage (HIU)  
Helmholtzstraße 11, 89081 Ulm, Germany

A. Latz  
Institute of Electrochemistry  
Ulm University  
Albert-Einstein-Allee 47, 89081 Ulm, Germany

 Supporting information for this article is available on the WWW under https://doi.org/10.1002/batt.202500321

 © 2025 The Author(s). *Batteries & Supercaps* published by Wiley-VCH GmbH. This is an open access article under the terms of the Creative Commons Attribution License, which permits use, distribution and reproduction in any medium, provided the original work is properly cited.

electronic conductivity  $1.0 \times 10^{-4} \text{ S cm}^{-1}$ ) and LPSCI, quantifying their ionic and electronic conductivity. As a result, an electronic conductivity of  $5.56 \times 10^{-7} \text{ S cm}^{-1}$  and an ionic conductivity of  $1.66 \times 10^{-7} \text{ S cm}^{-1}$  were determined for a mixture with 42 vol% (70 wt%) NMC622.<sup>[7]</sup>

Only a limited number of studies have considered the use of coated active material with low intrinsic electronic conductivity. Furthermore, there has been no emphasis placed on the characterization of charge transport with respect to coated active material<sup>[20–22]</sup> but on degradation and aging behavior of CCs.

In order to counteract the low electronic conductivity of the coated active material, it is possible to either increase the total proportion of active material in the microstructure or CA can be added. The latter has the advantage of increasing the electronic conductivity, even with small quantities (wt%), but it has the disadvantage of causing degradation at the CA-SE interfaces and reducing the fraction of active material or SE, which in turn negatively affects either the capacity or ionic conductivity of the CC.

To maintain a minimal quantity of CA, it is essential to consider the NMC:CA ratio, as they complement each other in the formation of electronic conducting pathways. For this reason, microstructures with low active material content should be supported with more CA content to form electronic pathways compared to those with high amounts of active material content in which the network of NMC particles contribute to the electronic conductivity of the CC. In our previous study, we investigated the electronic and ionic conduction mechanisms of mixtures of LPSCI as an SE and C65 as a CA. Our findings revealed that the percolation threshold is in the range of 3–4 wt% C65, leading to a high electronic conductivity of the compound without a significant impact on ionic conductivity.<sup>[23]</sup> Such a mixture could work as a conductive matrix (CM) for CCs that employ active material with low electronic conductivity. In this context, the term CM refers specifically to a pre-formed functionalized SE by adding CA above the percolation threshold. In doing so, the SE, respectively, the mixture of SE and CA becomes electronically conductive while maintaining its ionic conductivity. When adding CAM to this mixture of SE and CA, one could think of this mixture acting as a CM in which the CA is embedded. This is distinct from considering the entire composite electrode as a homogeneous CM. The CM approach is particularly relevant when using active materials that exhibit low intrinsic electronic conductivity or possess passivating or functional surface coatings, which can hinder charge transport.

Accordingly, the present study employs this CM to examine the relationship between microstructure and ionic/electronic conductivity in CCs, as well as their electrochemical performance in terms of capacity and rate capability. To this end, the weight ratio between LPSCI and C65 was maintained at 96:4 in all various CCs, while the proportion of the coated-NMC622 was varied in between 50 and 80 wt%. The microstructural evolution of different cathode mixtures was analyzed, and the effective ionic and electronic conductivities were investigated experimentally, supported by numerical simulations based on reconstructions of the tomography data. Subsequently, these findings were correlated with the rate capability and cycling performance of the cells. The results of this study contribute to a better understanding of

the interplay between microstructure, partial conductivities and electrochemical performance of CCs with various compositions.

## 2. Experimental Section

### 2.1. Material Synthesis and Cell Preparation

$\text{Li}_6\text{PS}_5\text{Cl}$  was synthesized using a previously reported solid-state reaction route<sup>[23,24]</sup> and ground in an agate mortar to reduce the size of the particles (more information on SE pregrinding can be found in Figure S1, Supporting Information). Pre-ground LPSCI was mixed with C65 (MTI, Imerys, Bironico, Switzerland) and single crystal NMC622 coated with a ceramic Li-ion-conductor in nm-range (CAM) simultaneously to prepare the CC mixtures, whereby the weight ratio of LPSCI to C65 was kept constant at 96:4 for all CC compositions.<sup>[23]</sup> Physical properties of the materials can be found in the Table T1, Supporting Information.

The CC mixtures were prepared in a ball mill (Pulverisette 7, Fritsch GmbH, Germany) with 5 mm diameter  $\text{ZrO}_2$  grinding media at a rotational speed of 160 rpm and a total milling time of 1 h. The milling media to powder ratio was 29.74:1. The CC mixtures and their composition are given in Table 1. Due to the introduction of the CM in the CC, the content of C65 varies in the mixtures according to the coated-NMC622 fraction.

For electrochemical impedance spectroscopy (EIS) measurements, CC pellets were manufactured by uniaxially pressing 100 mg of CC mixture in a die with an inner diameter of 10 mm under 375 MPa for conductivity measurements. Additionally, because both coated-NMC622 and C65 contribute to the formation of the electronic pathways, the intrinsic conductivity of coated-NMC622 + C65 mixtures in CC was determined by considering the C65 share in electronically conductive phase in the corresponding CC mixtures. The thickness and densities of individual samples used for electrochemical characterization can be found in Table T2, Supporting Information.

For the preparation of ASSB cells with a diameter of 10 mm, 85 mg of LPSCI were compacted with a uniaxial pressure of 375 MPa as a separator layer of  $\approx 730 \mu\text{m}$  thickness corresponding to an electrolyte mass loading for the separator of  $106.23 \text{ mg cm}^{-2}$ . Subsequently, 20 mg CAM mixture (e.g., for the 70 wt% mixture, this corresponds to a total mass loading of  $\approx 17.83 \text{ mg cm}^{-2}$ , corresponding to a CAM loading of  $2.67 \text{ Ah cm}^{-2}$ ) were applied on one side of the LPSCI separator and the In/InLi alloy as an anode to the other side. For the anode, 6 mm-diameter lithium

Table 1. Examined CC mixtures with the weight and volume fractions.

Mixtures	wt%			vol%		
	CAM	CM	C65	NMC622	LPSCI	C65
CAM : CM	NMC622	LPSCI	C65	NMC622	LPSCI	C65
0:100	0.00	96.00	4.00	0.00	95.36	4.64
50:50	50.00	48.00	2.00	28.54	68.14	3.32
70:30	70.00	28.80	1.20	48.24	49.35	2.40
80:20	80.00	19.20	0.80	61.51	36.71	1.79
						38.50

foils (200 µm thick) and 8 mm-diameter indium foils (250 µm thick) were stacked prior to cell assembly. The resulting anode assembly had Li fraction of 35.06 at%. The total mass of the stack was approx. 95 mg, corresponding to a mass loading of 121 mg cm<sup>-2</sup>.

## 2.2. Material Characterization

Microstructural characterization of the CC pellets was performed using a scanning electron microscope (SEM) (Zeiss Sigma 300VP & Zeiss Crossbeam 550, Carl Zeiss Microscopy GmbH, Germany) with secondary (SE) and backscattered electron (BSE) detectors. For 2D SEM analyses, cross sections of the CC pellets were prepared by using an argon polisher (ArBlade 5000, Hitachi, Japan), and the surface was sputtered with gold. FIB/SEM tomography was performed using a gallium liquid metal ion source (Ga LMIS), and these analyses include the procedure of fs-laser precutting of the region of interest, ion sectioning with simultaneous SEM imaging. Serial sectioning was done with an ion beam current of 3 nA and an accelerating voltage of 30 kV. SEM imaging was performed using an Inlens backscattered (ESB) detector at 1.5 kV accelerating voltage and 1 nA beam current. The procedure for image processing of the acquired image stacks from FIB/SEM-tomography includes alignment (3D reconstruction), cropping to a region of interest, followed by AI image segmentation with a deep neural network. Reconstruction and segmentation were done with Dragonfly software. Transfer shuttles of Kammerath & Weiss (Schwerin, Germany) for SEM and of Zeiss (Carl Zeiss Microscopy GmbH, Germany) for FIB/SEM-tomography were used to transport the samples to the microscope chamber to protect them from ambient atmosphere.

## 2.3. Electrochemical Tests

All electrochemical tests were performed in a climate chamber (KB 53, BINDER GmbH, Germany) at 25 °C on a potentiostat (Biologic VSP 300, Seyssinet-Pariset, France). Electrochemical impedance spectroscopy (EIS) measurements were conducted using blocking cell configurations to determine electronic and ionic conductivity with an oscillation amplitude of 10 mV in the frequency range between 7 MHz and 5 mHz. For the ion blocking configuration, stainless steel plungers were used as electrodes while in electron blocking configuration, LPSCl powder and In(InLi)<sub>x</sub> alloys with x < 0.45 as lithium reservoirs on both sides of the CC pellet were used in a setup applying 40 MPa (demonstrated in Figure S2, Supporting Information). For each investigated pellet, three identical measurements were performed. The resulting impedance spectra were analyzed by fitting with a T-type transmission line model (TLM) based on the literature<sup>[25,26]</sup> using the RelaxIS 3 software package (rhd Instruments, Darmstadt, Germany). The effective conductivity of the CC is calculated by using the geometrical thickness L and area A of the cylindrical composite cathode and the calculated resistances R<sub>el</sub> and R<sub>ion</sub> obtained from the impedance analysis (Equation (1)).

$$\sigma_{\text{el/ion, eff}} = \frac{L}{R_{\text{el/ion}}} \quad (1)$$

The additional contribution of ionic resistance across the interface of two In/(InLi)<sub>x</sub> electrodes and two LPSCl blocking layers was determined experimentally and considered for the interpretation of the EIS data of the CC mixtures. (Figure S3, Supporting Information).

The tortuosity factor was calculated considering both the effective partial conductivity of the sample and the conductivity of the electronic phase (for the electronic tortuosity) or the ionic phase (for the ionic tortuosity) and the volume fraction  $\varphi_{\text{el/ion}}$  of the respective material by using Equation (2).<sup>[27]</sup>

$$\tau_{\text{el/ion}}^2 = \frac{\sigma_{\text{el/ion,0}}}{\sigma_{\text{el/ion, eff}}} \varphi_{\text{el/ion}} \quad (2)$$

Cycling experiments were carried out in a voltage range between 1.88 and 3.63 V. After a formation cycle of C/10, the cells were cycled in constant current and constant voltage modes with C-rates between C/5 and 1C. For the calculation of the C-rate, a theoretical capacity of the CAM of 150 mAh g<sup>-1</sup> was assumed. During cycling, a stack pressure of 40 MPa was applied. For information regarding reproducibility of the cycling experiments, please refer to the Figure S7, Supporting Information.

## 2.4. Modeling and Simulation

Effective conductivity calculations for ionically and electronically conducting phases have been performed using the battery and electrochemistry simulation tool BEST. The electronic conductivity is calculated on a representative cut-out of the reconstruction data of CC samples with different CAM content. These simulations are carried out directly on the experimentally reconstructed 3D microstructures obtained via FIB-SEM tomography, ensuring that the real particle arrangements and phase distributions are represented. These cut-outs are selected to have the same volume fraction of active material as given in Table 2. The dimension of these domains is the full thickness of the reconstruction in through direction and 14 µm in the lateral directions. Within these cut-outs the active material particles were identified using a watershed algorithm implemented in MATLAB based on Ref. [28] To obtain the electronic or ionic conductivity, the Poisson equation is solved with varying local conductivity through a finite-volume discretization.

$$0 = \nabla \cdot (\sigma_{\text{el/ion,0}}(\mathbf{x}) \nabla \varphi_{\text{el/ion}}(\mathbf{x})) \quad (3)$$

Boundary conditions were chosen to reproduce the ionically or electronically blocking measurement setups schematically shown in Figure 3. Details of the approach are described in more detail in Ref. [29] Local ionic and electronic conductivities were set according to the phase segmentation assuming different geometric scenarios arising from the processing of materials as schematically indicated in Figure 5. The contact resistance between active material particles is added to the electrical current at the corresponding interfaces and described through the specific contact resistance  $\rho_{a,b}^{CR}$ . The electrical current at the contact interface between two active particles is therefore

given by  $\vec{j} = -\left(\bar{\sigma}_{a,b} + \frac{d}{\rho_{a,b}^{CR}}\right) \cdot \vec{\nabla}\varphi$ . The value of the specific contact resistance ( $50 \Omega\text{cm}^2$ ) was chosen to reproduce experimental data at 70 wt% CAM content in an electrode without CA.

### 3. Results and Discussion

#### 3.1. Microstructural Investigation

The cross-sectional SEM images of the CCs with various CAM fraction in **Figure 1** demonstrate that the particle size distribution of

the CAM (equiaxed grains in light gray) is relatively narrow, while the LPSCl (dark gray) exhibits large agglomerates. Furthermore, the composite cathode exhibits a relatively dense packing, which can be attributed to the plasticity and low Young's modulus of the LPSCl, coupled with the high pressure applied.<sup>[30]</sup>

3D volume images of the various CCs taken by FIB/SEM tomography confirm the 2D results with regard to the phase distribution (see **Figure 2a–c**. The lower the amount of CAM, the more pronounced the SE network. Phase segmentation images are presented in **Figure 2d–f**, which show three distinct phases: coated-NMC622 (red), LPSCl (green), and pores (blue), while the C65 cannot

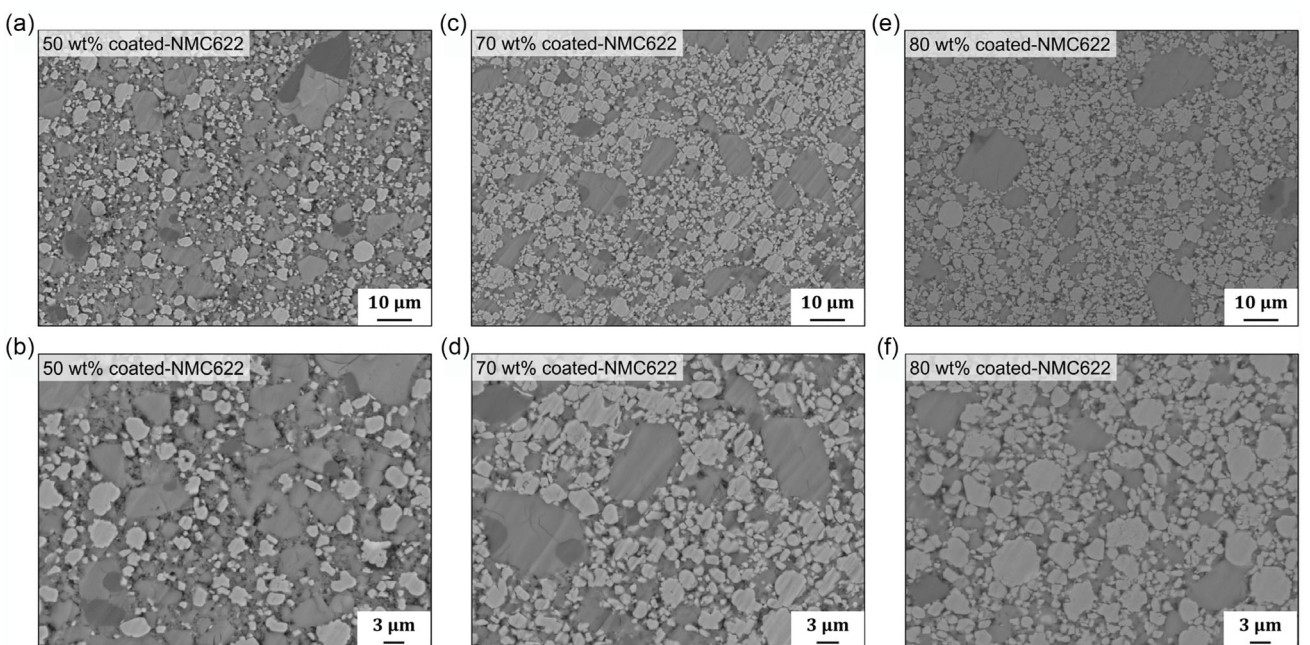


**Figure 1.** Cross-sectional SEM BSE images of a,b) 50 wt% CAM with CM, c,d) 70 wt% CAM with CM, and e,f) 80 wt% CAM with CM in CC pellets. CAM is shown in light color. LPSCl is given by the dark particles.

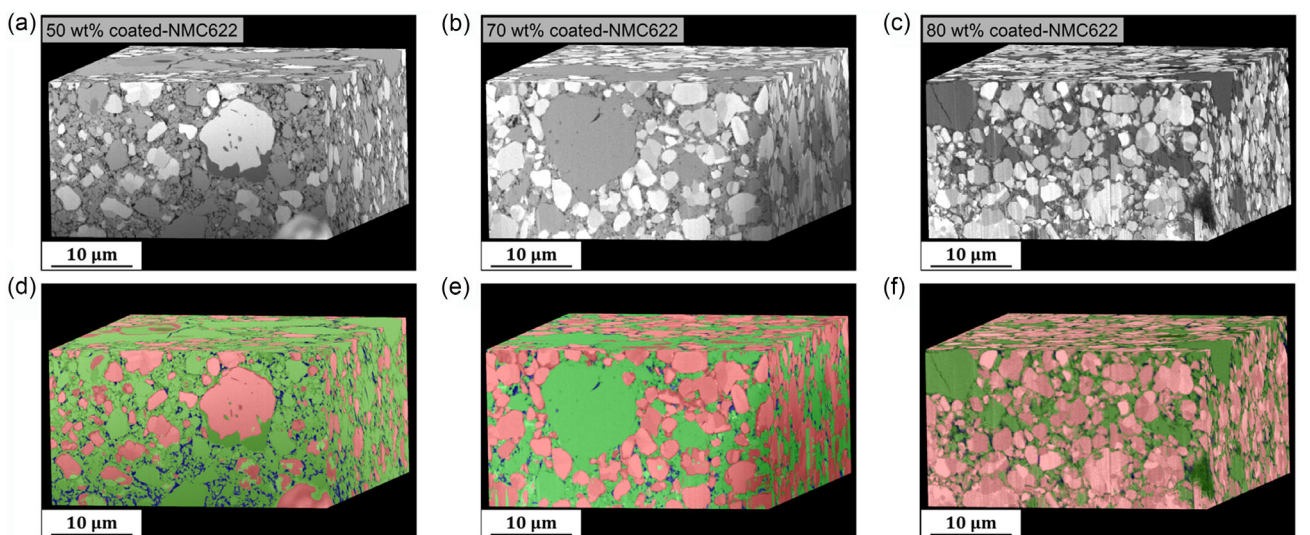


**Figure 2.** 3D microstructures obtained with FIB-tomography (50, 70, and 80 wt% CAM). The voxel resolution is  $26 \times 26 \times 50 \text{ nm}$ . a–c) original grayscale data from FIB-tomography; d–f) segmented tomographs, with LPSCl in green, CAM in red and pores in blue.

Table 2. Comparison of the designed composition and FIB-tomography segmentation results.					
CAM:CM (wt%)	CAM:CM (vol%)	Segmentation (vol% components in CC)			
		Red	Green	Blue	
		CAM	LPSCI	Pores	
50.0 : 50.0	28.5 : 71.5	29.95	66.73	3.22	
70.0 : 30.0	48.2 : 51.8	47.15	48.26	4.60	
80.0 : 20.0	61.5 : 38.5	51.93	42.36	5.71	

be resolved. The phase fractions obtained from the segmented 3D volumes are approximately in line with the initial composition (**Table 2**). Note that those values are based on the segmentation of a small volume of the sample, and thus do not necessarily represent the whole sample, which is by nature inhomogeneous in its composition. Additionally, C65 amounts were not considered as it was not possible to detect them on the volume images.

### 3.2. Electronic and Ionic Conductivities

**Figure 3** illustrates the representative Nyquist plots of the respective CCs (50 wt% CAM, gray; 70 wt%, red; 80 wt%, blue circles) in ion blocking and electron blocking configuration, with measured impedance presented as markers and the equivalent-circuit fit as a solid line. The CC pellets and the associated TLM model are shown in a) ion blocking configuration for electronic conductivity, b) electron blocking configuration for ionic conductivity, and c) circuit elements applied in the utilized TLMs for the respective charge pathways (in light blue illustrated the electronic bulk resistance corresponding to an ohmic resistor and in dark blue the electronic interface impedance corresponding to a ZARC element, please refer to Figure S6, Supporting Information for further details of the used TLM). Additionally, the associated TLM model and the equivalent circuit elements applied in the model are provided according to Ref. [27] As the CCs consist of multiple phases, charge transport can occur within these phases and across the interface between them. Consequently, the TLM model depicted in Figure 3 encompasses all these contributions ( $Z_{el}$ ,  $Z_{ion}$ , and  $Z_{int}$ ) on the impedance spectra.

The low-frequency part ( $\omega \rightarrow 0$  Hz) of the Nyquist plot performed with ion-blocking electrodes shown in Figure 3a indicates a teardrop shape for the samples containing 70 and 80 wt% CAM. This is a characteristic behavior of a percolating electronic network.<sup>[7,27]</sup> In contrary, this is not the case when the amount of cathode active material was reduced to 50 wt%, indicating a low electronic conductivity. In contrast, Nyquist plots with electron-blocking electrodes in Figure 3b emphasize ionic transport and interfacial phenomena, with blocking of electron transport at the electrodes (In/Li interfaces) with well-defined visible semi-circles in the mid-to-high frequency range, which is attributed to bulk and interfacial ionic resistances in CCs. At 50 wt% CAM, the impedance is the lowest, suggesting good ionic connectivity—likely due to a higher fraction of the ionically conductive phase (SE). As the CAM fraction increases to 70 wt%

and especially 80 wt%, impedance increases again, pointing to reduced ionic percolation due to the collapse of the SE network.

**Figure 4** shows the effective ionic and electronic conductivity and the corresponding tortuosity values of the different CCs as well as of the CM and the CAM.

The pure CM (corresponding to 0% CAM) consists of 96 wt% LPSCI and 4 wt% C65 and exhibits a high effective electronic conductivity of  $2.71 \times 10^{-3} \text{ S cm}^{-1}$ , which is in line to our previous findings.<sup>[23]</sup> The corresponding impedance spectra can be found in Figure S4, Supporting Information. At the other end of the scale, samples containing only CAM exhibit an effective electronic conductivity of  $7.98 \times 10^{-5} \text{ S cm}^{-1}$  (see Figure S5, Supporting Information). This value is at the lower end of the reported values of electronic conductivity of NMC with similar Ni content in a range between  $10^{-6}$  and  $10^{-4} \text{ S cm}^{-1}$ <sup>[8,31,32]</sup> and can most likely be attributed to the use of passivation coating on the CAM in this study. Adding 50 wt% CAM to the CM, the effective electronic conductivity drops by 4 orders of magnitude to  $2.08 \times 10^{-7} \text{ S cm}^{-1}$ , this is accompanied with a sudden surge in tortuosity. Increasing the amount of CAM to 70 wt%, respectively, 80 wt% results in an increasing effective electronic conductivity, which ultimately converges toward the value of pure CAM. It is noteworthy that the absolute quantity of C65 diminishes concurrently with increasing amount of CAM (see Table 1). In other words, despite the fact that the mixture contains the greatest proportion of C65 (50 wt% coated-NMC622), it exhibits the lowest effective electronic conductivity ( $2.08 \times 10^{-7} \text{ S cm}^{-1}$ ). In contrast, the ionic conductivity (which is provided by the CM, respectively the SE) illustrated in Figure 4b is not as strongly influenced by the addition of CAM. The CC containing 50 wt% CAM exhibits approximately the same effective ionic conductivity as the pure CM. Even adding 80 wt% CAM reduces the effective ionic conductivity only by less than one order of magnitude to  $5.15 \times 10^{-5} \text{ S cm}^{-1}$  and the tortuosity factor increases from 1.00 (pure CM) to 11.86. These results indicate that the CM network remains intact providing conductive pathways for ions, even for a high CAM-content of 80 wt% corresponding to about 37 vol% of ionically conductive SE (see Table 1). It can be assumed that due to its plasticity, the LPSCI particles adapt to the surrounding CAM particles under high pressure during fabrication providing a conductive network even with such low phase fractions.<sup>[33]</sup>

In contrast—and surprisingly—the effective electronically conductive network of the CM collapses with the addition of 50 wt% CAM, but is re-established by further increasing the CAM content in the CC. We assume that the C65 partially adheres to the CAM particles during the preparation of the CC mixture. As a result, the amount of C65 in the CM drops below the percolation threshold of 3–4 wt%, and the CM becomes electronically insulating as shown in our previous work.<sup>[23]</sup> In turn, 50 wt% of CAM is not enough to build a conductive network of CAM particles resulting in a very low effective electronic conductivity of the CC. As the amount of CAM increases, we exceed the percolation threshold of the CAM, and an electronically conductive CAM network is formed, with the CAM taking over the role of the primary electron conductor. This hypothesis is supported by microscopic investigations (see Figure 1 and 2) as well as by the Nyquist plots which indicate that there is no percolation network for the 50 wt% sample.

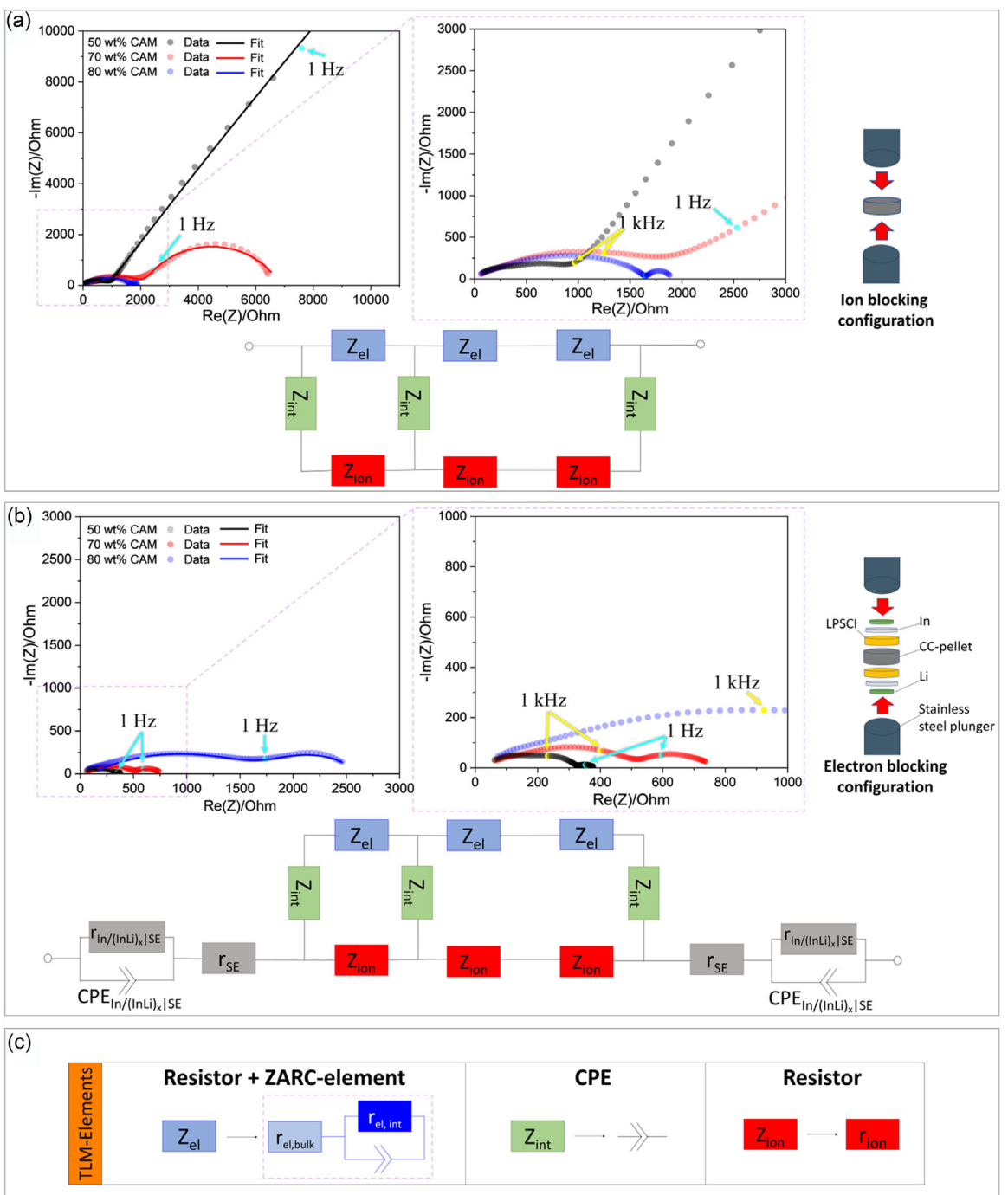


**Figure 3.** Nyquist plots of CC pellets (measured impedance shown as markers and equivalent circuit fit as a solid line) and associated TLM model a) ion blocking configuration for electronic conductivity, b) electron blocking configuration for ionic conductivity, and c) circuit elements applied in the utilized TLMs for the respective charge pathways (in light blue illustrated the electronic bulk resistance corresponding to an ohmic resistor and in dark blue the electronic interface impedance corresponding to a ZARC-element).

**Figure 5** illustrates the numerical simulation of the effective electronic conductivity for different compositions and with different assumptions as described in the experimental part. The results support our hypothesis of changes in the electronic network due to CC processing. The blue data points represent the experimental values according to Figure 4a. The simulations assume and evaluate different scenarios of C65 distribution within the CC schematically indicated on the right-hand side of Figure 5 and applied to

the segmented image data with different CAM contents. Scenario i) represents a homogeneous distribution of C65 in the CM. The latter being the ideal case for forming percolating ionic and electronic conducting networks throughout the CC. Scenario ii) assumes that after processing all the C65 sticks to the surface of CAM particles providing a closed conductive coating (green circles). The CM is not contributing to the electronic conduction in this case. Scenario iii) represents a mixture without

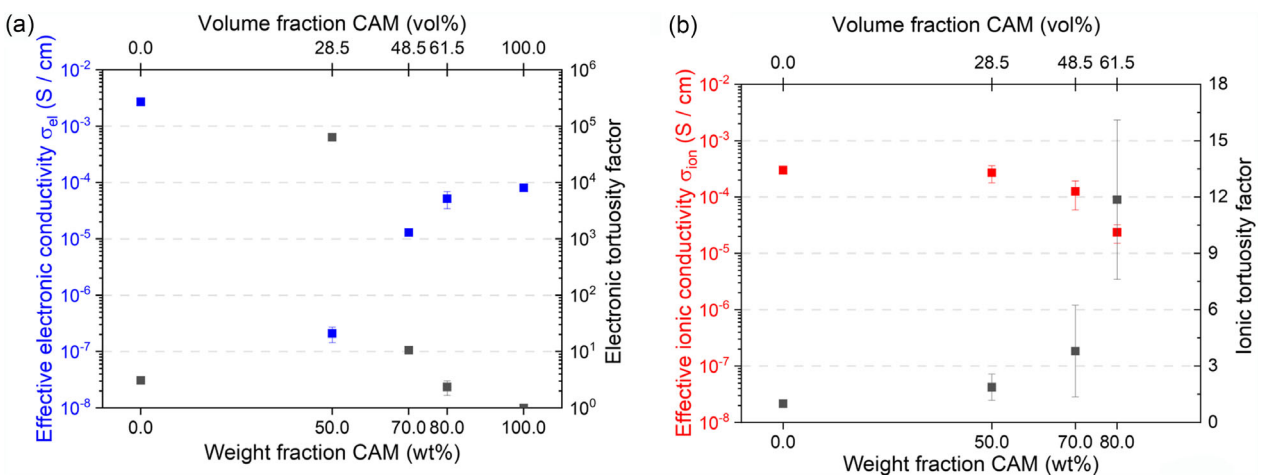


Figure 4. a) Effective electronic conductivity and tortuosity factor and b) effective ionic conductivity and tortuosity factor of CC mixtures.

**Table 3.** Values of electronic and ionic conductivity with corresponding tortuosity factors for different CAM fractions.

Weight fraction CAM [wt%]	0.00	50.00	70.00	80.00	100.00
Volume fraction CAM [vol%]	0.00	28.54	48.54	61.51	100.00
$\sigma_{el}$ [S cm $^{-1}$ ]	$2.71 \times 10^{-3}$	$2.08 \times 10^{-7}$	$1.29 \times 10^{-5}$	$5.15 \times 10^{-5}$	$7.98 \times 10^{-5}$
El. tortuosity factor	3.09	63477.89	10.57	2.35	1.00
$\sigma_{ion}$ [S cm $^{-1}$ ]	$3.00 \times 10^{-4}$	$2.69 \times 10^{-4}$	$1.25 \times 10^{-4}$	$2.37 \times 10^{-5}$	—
Ion. tortuosity factor	1	1.88	3.80	11.86	—

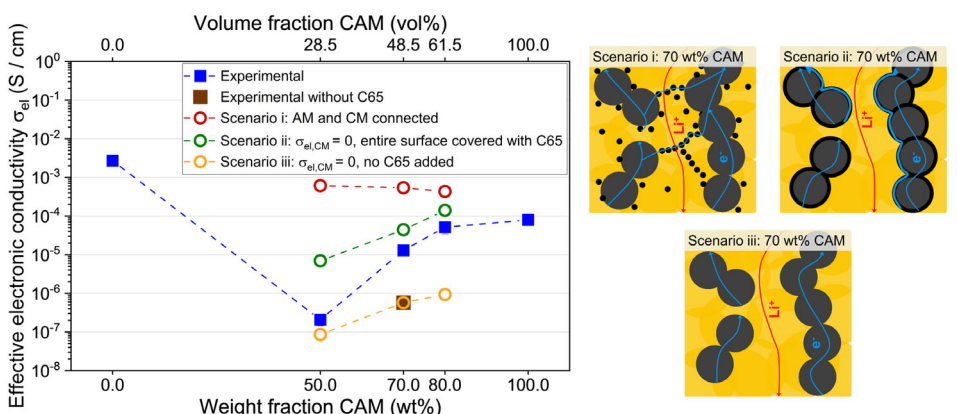


Figure 5. Microstructure-resolved simulation of the electronic conductivity for different mixtures and different assumptions in comparison to experimental findings. Additionally, the simulated scenarios are shown schematically.

C65 CA. Note that all of the scenarios are simplifications aiming to understand the effect of limiting processes. Future work will provide a more comprehensive description of C65 networks.

Red circles in Figure 5 represent the ideal scenario i) in which the C65 content in the CM is at the percolation threshold—and thus, the CM is electronically conductive for all CC mixtures—and the CM phase is fully connected to the CAM phase. Simulations predict that the effective conductivity slightly decreases with increasing CAM content due to the lower electronic conductivity of the CAM compared to the CM. This is in contrast to the experimental data (blue squares) where effective electronic

conductivity drops significantly on addition of 50 wt% CAM and then rises again considerably with increasing CAM content. An additional measurement of a CC mixture containing 70 wt% CAM and pure SE (without C65) was performed. The effective electronic conductivity of measurements of the electrode without C65 is lower by two orders of magnitude. The measured conductivity (without C65) is used to identify the value of the specific contact resistance between CAM particles, which is used for all other numerical simulations. Additionally, we virtually test in scenario iii) a CM without C65 additive (yellow circles). Conductivity values predicted by the simulations are lower for all compositions.

This demonstrates that addition of C65 to the CM has a significant effect on the measured electrode electronic conductivity. Finally, we virtually probe the hypothesis of C65 adhesion on CAM particle surfaces during processing. In scenario ii) C65 completely covers the surface of the CAM particles, while the CM loses any electric conductivity. The highly conductive surface film forms a percolating network via the CAM particle network, which results in very high CC effective electronic conductivity. Experiments with C65 in the CM are between scenario iii) without C65 and scenario ii) assuming perfect coverage. Based on the simulation studies, we can conclude that the C65 has a strong positive effect on electronic conduction networks. However, adding CAM to the CC formulation affects the electric network and reduces the effective conductivity compared to the ideal C65 distribution in the CM alone. Adhesion of the C65 to the CAM forming imperfect partial conductive networks on the particle surface or within the CM is a very probable scenario to explain the observed behavior.

Furthermore, our findings are consistent with the predictions of Bielefeld et al. showing that the effective ionic conductivity of a CC is less susceptible to the addition of CAM compared to effective electronic conductivity.<sup>[6]</sup> Virtually varying the CAM (assumed to be electronically conductive) and SE (assumed to be electronically nonconductive but ionically conductive) ratios between 40 and 70 vol%, the authors observed a consistently high utilization level of SE particles between 80 and 100 vol%, indicating minimal changes in ionic conductivity across this range of mixtures. In contrast, the utilization level of the CAM particles exhibited a much broader range, varying between 0 and 100 vol%, suggesting significant alterations in electronic conductivity.

### 3.3. Cell Performance

To assess the electrochemical performance of the various compositions and to reveal the contributions of the effective electronic and ionic conductivity on it, half-cells were cycled at different C-rates. Figure 6 a illustrates the initial charge and discharge curves obtained at C/10 as the formation cycle. The mixture with 50 wt% CAM exhibits only negligible capacity at C/10 (and is therefore not plotted in the subsequent figure, but is shown in Figure S7, Supporting Information), which we attribute to severe kinetic

limitations due to the very low electronic conductivity even at low C-rates. According to Hendriks et al. at lower rates, even unbalanced transport can lead to a full CAM utilization as long percolation is ensured and pathways for the ionic and electronic transport coexist.<sup>[20]</sup> However, based on our EIS data, we assume that the electronic percolation network has collapsed by “extracting” the C65 from the CM and no alternative electronically conductive network consisting of the CAM particles has formed due to the low amount of CAM. The composite cathode with 70 wt% CAM has a specific discharge capacity of 99.8 mAh g<sup>-1</sup>, whereas the cathode with 80 wt% displays a reduced specific discharge capacity of 51.2 mAh g<sup>-1</sup> (Figure 6a).

After formation at C/10, we gradually increased the C-rate up to 1C and concluded the C-rate test with a final step at C/5 to investigate potential ageing due to cycling. Figure 6b highlights that the CCs with 70 wt% CAM consistently exhibit a higher capacity at all C-rates compared to the mixtures with 80 wt% CAM. However, both CC mixtures experience a capacity decrease through higher C-rates. While the capacity of the 80 wt% electrodes diminishes rapidly with increasing C-rate, the samples with 70 wt% CAM demonstrate a minimum of 25% of the initial capacity at C/2. Notably, for both CC mixtures, the initial capacity at C/5 is closely aligned with the capacity at C/5 at the end of the rate capability test, indicating the absence of cycling-related aging and degradation during the initial 15 cycles.

Figure 7 summarizes all the results by showing the effective partial conductivities of the various CC mixtures and correlating them with the half-cell capacities of the respective cells at C-rates of C/10 and C/5. Assuming that the best performance of an electrode can be expected having balanced ionic and electronic conductivity, the most beneficial CC mixture in our set-up would be in the range of 75 wt% CAM. As mentioned before, in a recent study using a blend of LiMn<sub>2</sub>O<sub>4</sub>/Li<sub>3</sub>InCl<sub>6</sub> for the composite cathode, Hendriks et al. have shown that the highest capacity is achieved at a  $\sigma_{\text{ion}}/\sigma_{\text{el}}$ -ratio of about 0.2 at a C-rate of C/10. They point out that the balancing of  $\sigma_{\text{ion}}$  and  $\sigma_{\text{el}}$  is of little importance at low C-rates (as long as some conductivity is given), but becomes increasingly important and determines the capacity with increasing current density.<sup>[19]</sup> This is consistent with our results, which show that for the CC mixture containing 70 wt% CAM, 84% of the capacity

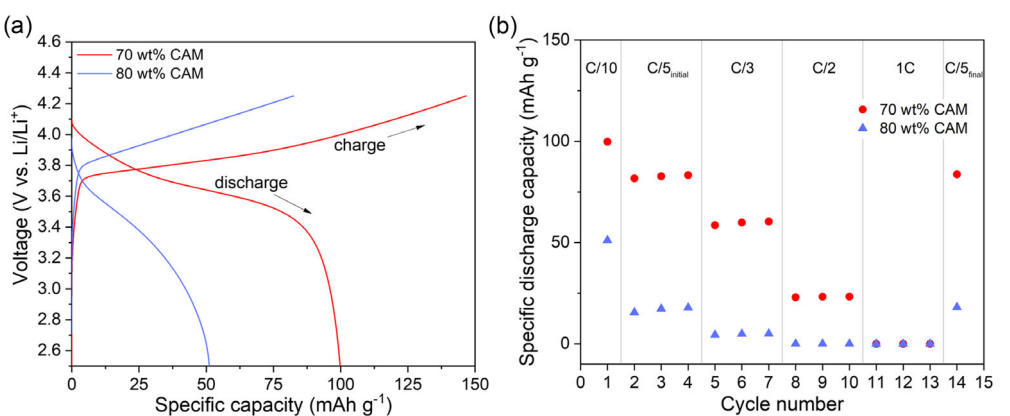


**Figure 6.** Electrochemical performance of composite cathodes with cutoff voltages of 4.25 and 2.50 V. a) charge/discharge-curves during formation at C/10 and b) C-rate capability test up to 1C.

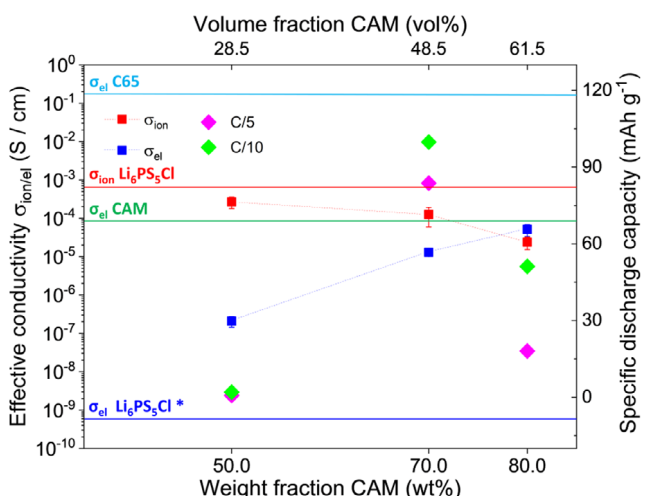


**Figure 7.** Effective partial conductivities (ionic: red-square; electronic: blue-squares) from composite cathode mixtures with various CAM content. The discharge capacities obtained at a discharge current of C/10 and C/5 with cutoff voltages of 4.25 and 2.50 V are plotted with diamonds. In addition, the partial conductivities of pure CAM, pure solid electrolyte (SE) and C65 are plotted, electronic conductivity of SE taken from literature (\*<sup>[34,35]</sup>).

at C/10 can be achieved at a rate of C/5, whereas the mixture containing 80 wt% CAM achieves only 35% at C/5.

#### 4. Conclusion

The study demonstrates that the performance of CCs is significantly influenced by the balance between ionic and electronic conductivity, which depends on the weight fraction of cathode active material and the distribution of the CA which was C65 in this study.

A schematic sketch (**Figure 8**) summarizing the conduction behavior of the different composite cathode is provided, illustrating the evolution of the electronic and ionic pathways as CAM content increases:

At 0 wt% CAM, 4 wt% C65 is sufficient to be at the percolation threshold and ensure high electronic conductivity of the so-called CM. At the same time, the ionic conductivity is high as well since the network of SE is well established and negligibly impaired by the network of C65.

When adding CAM to the CM, we assume that considerable fragments of the CA adhere to the surface of the CAM particles. As a result, the amount of C65 in the CM falls below the percolation

threshold and the electronic conductivity collapses at 50 wt% CAM. As a result, the capacity of such an electrode is negligible even at low C-rates—even though the ionic conductivity is high.

An increase in the CAM content to 70 wt% was found to result in the re-establishment of the electronic conductivity of the CCs, indicating that the surface covered CAM particles have now formed a percolating network. Interestingly, the SE network remains intact, exhibiting ionic conductivity that approaches the level observed in the 50 wt% mixture. This suggests the attainment of a balance between electronic and ionic pathways, as evidenced by the high specific discharge capacity and rate capability.

As expected, a further increase in the CAM content to 80 wt% leads to a further improvement in the electronic conductivity. However, a decline in the ionic conductivity is now evident, as the ionic conductive pathways are presumably impeded by the elevated CAM content. Consequently, a reduction in the electrochemical performance of the CCs is observed, which becomes more pronounced as the C-rate increases. Evidently, the decline in ionic conductivity overcompensates the further increase in electronic conductivity.

These findings show that the loss of CA in the CM must be considered when producing three-phase cathode mixtures. How much of the CA adheres to the surface of the CAM particles depends on various factors such as the specific surface area of the CAM particles, the structure of the CA, or the mixing process. The question of how much CAM is required to form a percolation network also depends on similar factors. In this study, it was >50 wt%.

In summary, this work provides a comprehensive understanding of how composition, microstructure, and transport properties interact and how this influences the performance of CCs. These insights contribute to guide the design of advanced solid-state batteries with improved capacity and rate capability by tailoring the composition of the cathode mixture to achieve balanced transport properties.

#### Acknowledgements

This research was funded by the German Federal Ministry of Education and Research within the program "FH-Impuls" (Project SmartPro, Subproject Smart-BAT, Grant no. 13FH41071A). Publication funded by Aalen University of Applied Sciences and Deutsche Forschungsgemeinschaft (DFG, German Research Foundation). The authors acknowledge support by the state of Baden-Württemberg through bwHPC and the German Research Foundation (DFG) through grant no INST 40/575-1

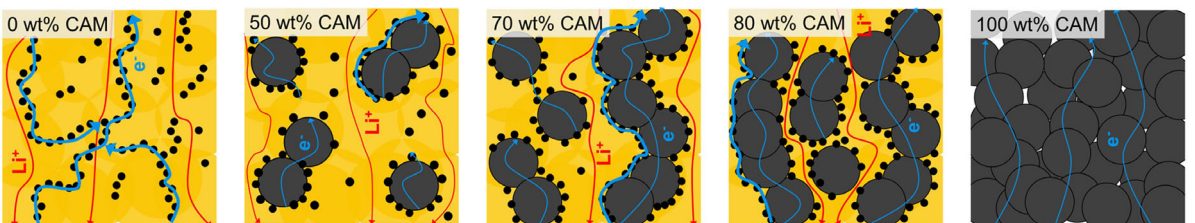


**Figure 8.** Schematic representation of the composite cathode microstructure with an increasing fraction of CAM. 0 wt% CAM: C65 content 4 wt% at the percolation threshold, electronically conductive.

FUGG (JUSTUS 2 cluster). The authors gratefully acknowledge the financial support by the German Federal Ministry of Research and Education (BMBF) within the scope of the projects FestBatt2 (FKZ: 03XP0435A). The present article contributes to the research performed at CELEST (Center for Electrochemical Energy Storage Ulm-Karlsruhe).

Open Access funding enabled and organized by Projekt DEAL.

## Conflict of Interest

The authors declare no conflict of interest.

## Data Availability Statement

The data that support the findings of this study are available from the corresponding author upon reasonable request.

**Keywords:** composite cathodes · conductivity · microstructure · solid-state batteries

- [1] Y. Xiao, Y. Wang, S.-H. Bo, J. C. Kim, L. J. Miara, G. Ceder, *Nat. Rev. Mater.* **2020**, *5*, 105.
- [2] J. Kim, M. J. Kim, J. Kim, J. W. Lee, J. Park, S. E. Wang, S. Lee, Y. C. Kang, U. Paik, D. S. Jung, T. Song, *Adv. Funct. Mater.* **2023**, *33*, 2211355.
- [3] Y.-G. Lee, S. Fujiki, C. Jung, N. Suzuki, N. Yashiro, R. Omoda, D.-S. Ko, T. Shiratsuchi, T. Sugimoto, S. Ryu, J. H. Ku, T. Watanabe, Y. Park, Y. Aihara, D. Im, I. T. Han, *Nat. Energy* **2020**, *5*, 299.
- [4] J. Schnell, T. Günther, T. Knoche, C. Vieider, L. Köhler, A. Just, M. Keller, S. Passerini, G. Reinhart, *J. Power Sources* **2018**, *382*, 160.
- [5] K. J. Kim, M. Balaish, M. Wadaguchi, L. Kong, J. L. M. Rupp, *Adv. Energy Mater.* **2021**, *11*, 2002689.
- [6] A. Bielefeld, D. A. Weber, J. Janeck, *J. Phys. Chem. C* **2019**, *123*, 1626.
- [7] P. Minnmann, L. Quillman, S. Burkhardt, F. H. Richter, J. Janeck, *J. Electrochem. Soc.* **2021**, *168*, 40537.
- [8] R. Amin, Y.-M. Chiang, *J. Electrochem. Soc.* **2016**, *163*, A1512.
- [9] H. Lee, P. Oh, J. Kim, H. Cha, S. Chae, S. Lee, J. Cho, *Adv. Mater.* **2019**, *31*, e1900376.
- [10] J. C. Bachman, S. Muy, A. Grimaud, H.-H. Chang, N. Pour, S. F. Lux, O. Paschos, F. Maglia, S. Lupart, P. Lamp, L. Giordano, Y. Shao-Horn, *Chem. Rev.* **2016**, *116*, 140.
- [11] D. Karabelli, K. P. Birke, M. Weeber, *Batteries* **2021**, *7*, 18.
- [12] Y. Lee, J. Jeong, H. J. Lee, M. Kim, D. Han, H. Kim, J. M. Yuk, K.-W. Nam, K. Y. Chung, H.-G. Jung, S. Yu, *ACS Energy Lett.* **2022**, *7*, 171.
- [13] T. Nakamura, K. Amezawa, J. Kulisch, W. G. Zeier, J. Janeck, *ACS Appl. Mater. Interfaces* **2019**, *11*, 19968.
- [14] S. P. Culver, R. Koerver, W. G. Zeier, J. Janeck, *Adv. Energy Mater.* **2019**, *9*, 1900626.
- [15] C. Doerrner, I. Capone, S. Narayanan, J. Liu, C. R. M. Grovenor, M. Pasta, P. S. Grant, *ACS Appl. Mater. Interfaces* **2021**, *13*, 37809.
- [16] A.-Y. Kim, F. Strauss, T. Bartsch, J. H. Teo, J. Janeck, T. Brezesinski, *Sci. Rep.* **2021**, *11*, 5367.
- [17] F. Strauss, D. Stepien, J. Maibach, L. Pfaffmann, S. Indris, P. Hartmann, T. Brezesinski, *RSC Adv.* **2020**, *10*, 1114.
- [18] F. Walther, S. Randau, Y. Schneider, J. Sann, M. Rohnke, F. H. Richter, W. G. Zeier, J. Janeck, *Chem. Mater.* **2020**, *32*, 6123.
- [19] W. Zhang, T. Leichtweiß, S. P. Culver, R. Koerver, D. Das, D. A. Weber, W. G. Zeier, J. Janeck, *ACS Appl. Mater. Interfaces* **2017**, *9*, 35888.
- [20] T. A. Hendriks, M. A. Lange, E. M. Kiens, C. Baeumer, W. G. Zeier, *Batteries Supercaps* **2023**, *6*, e202200544.
- [21] S. Chida, A. Miura, N. C. Rosero-Navarro, M. Higuchi, N. H. Phuc, H. Muto, A. Matsuda, K. Tadanaga, *Ceram. Int.* **2018**, *44*, 742.
- [22] S. Randau, F. Walther, A. Neumann, Y. Schneider, R. S. Negi, B. Mogwitz, J. Sann, K. Becker-Steinberger, T. Danner, S. Hein, A. Latz, F. H. Richter, J. Janeck, *Chem. Mater.* **2021**, *33*, 1380.
- [23] E. Reisacher, P. Kaya, V. Knoblauch, *Batteries* **2023**, *9*, 595.
- [24] L. Zhou, N. Minafra, W. G. Zeier, L. F. Nazar, *Acc. Chem. Res.* **2021**, *54*, 2717.
- [25] Z. Siroma, N. Fujiwara, S. Yamazaki, M. Asahi, T. Nagai, T. Ioroi, *Electrochim. Acta* **2015**, *160*, 313.
- [26] Z. Siroma, T. Sato, T. Takeuchi, R. Nagai, A. Ota, T. Ioroi, *J. Power Sources* **2016**, *316*, 215.
- [27] L. Froboese, J. F. van der Sichel, T. Loellhoeffel, L. Helmers, A. Kwade, *J. Electrochem. Soc.* **2019**, *166*, A318.
- [28] A. Rabbani, S. Jamshidi, S. Salehi, *J. Petrol. Sci. Eng.* **2014**, *123*, 164.
- [29] E. Schlautmann, J. Drews, L. Ketter, M. A. Lange, T. Danner, A. Latz, W. G. Zeier, *ACS Energy Lett.* **2025**, *10*, 1664.
- [30] Z. Deng, Z. Wang, I.-H. Chu, J. Luo, S.-P. Ong, *J. Electrochem. Soc.* **2015**, *163*, A67.
- [31] H.-J. Noh, S. Youn, C. S. Yoon, Y.-K. Sun, *J. Power Sources* **2013**, *233*, 121.
- [32] S. Wang, M. Yan, Y. Li, C. Vinado, J. Yang, *J. Power Sources* **2018**, *393*, 75.
- [33] J.-M. Doux, Y. Yang, D. H. S. Tan, H. Nguyen, E. A. Wu, X. Wang, A. Banerjee, Y. S. Meng, *J. Mater. Chem. A* **2020**, *8*, 5049.
- [34] G. G. Serbessa, B. W. Taklu, Y. Nikodimos, N. T. Temesgen, Z. B. Muche, S. K. Merso, T.-I. Yeh, Y.-J. Liu, W.-S. Liao, C.-H. Wang, S.-H. Wu, W.-N. Su, C.-C. Yang, B. J. Hwang, *ACS Appl. Mater. Interfaces* **2024**, *16*, 10832.
- [35] J. M. Lee, Y. S. Park, J.-W. Moon, H. Hwang, *Front. Chem.* **2021**, *9*, 778057.

Manuscript received: April 28, 2025

Revised manuscript received: June 3, 2025

Version of record online: